Supplementary Information

Spatiotemporal analysis of periodontitis—the unique role of the IL-33/ST2 axis

Liu et al.

a

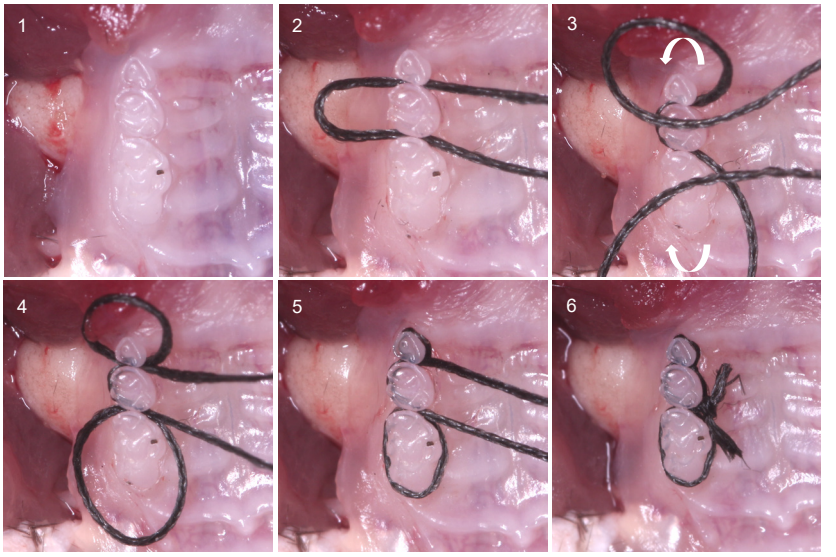

b

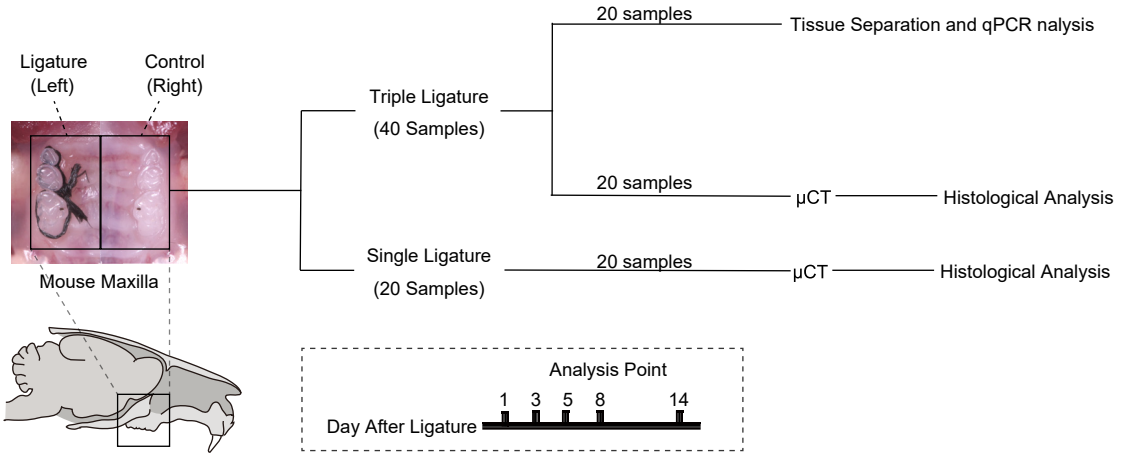

Supplementary Fig. 1 The experiment design and induction of the novel ligature model. | **a** Step-by-step instructions for the triple-ligature placement. More details are shown in Supplementary Video 1. **b** Experimental design and analysis time course.

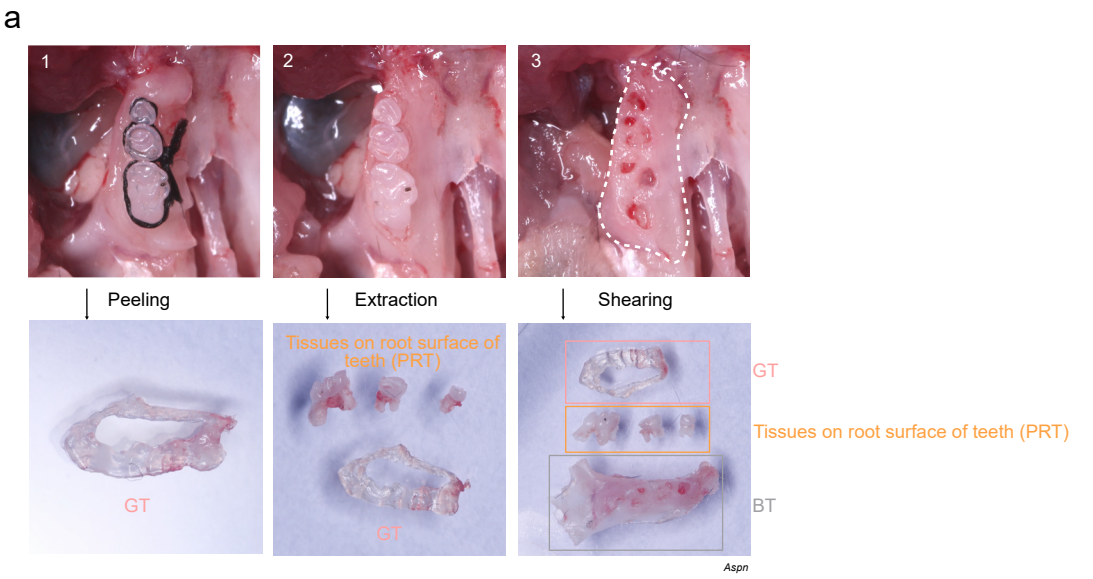

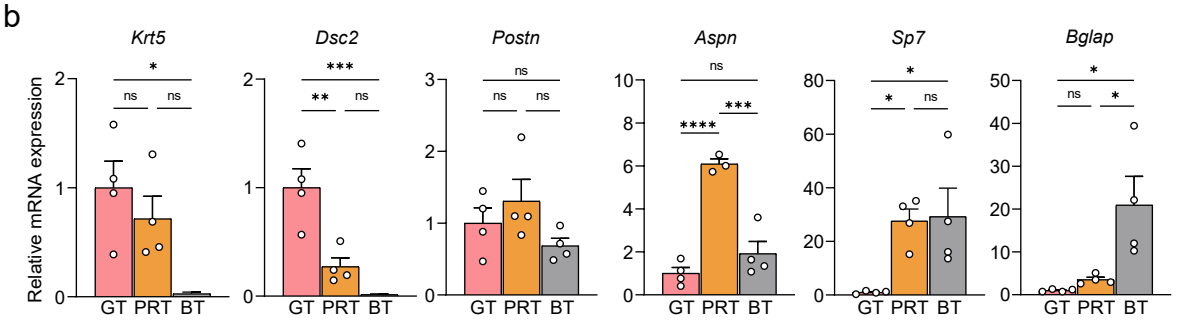

Supplementary Fig. 2 Distinct tissue separation via tissue-specific genes. | **a** Step-by-step instruction for tissue separation into GT, PRT, and BT. Separation was performed in the RNAlater or TRIzol in the actual experiments. GT: gingival tissue, PRT: peri-root tissue, BT: bone tissue. **b** mRNA expression of tissue-specific genes on the control side of the three tissues (on Day 8, GT = 1, *n* = 3 or 4). *Krt5* and *Dsc2* are for the verification of GT; *Postn* and *Aspn* are for PRT; *Sp7* and *Bglap* are for BT. Data are presented as the mean ± SEM. *P < 0.05; **P < 0.01; ***P < 0.001; ****P < 0.0001; ns, P > 0.05; by one-way ANOVA with multiple comparisons via Tukey's test. The obvious outliers were evaluated and excluded by Grubb's test (α = 0.05). The exact P values are shown in Supplementary Table 3.

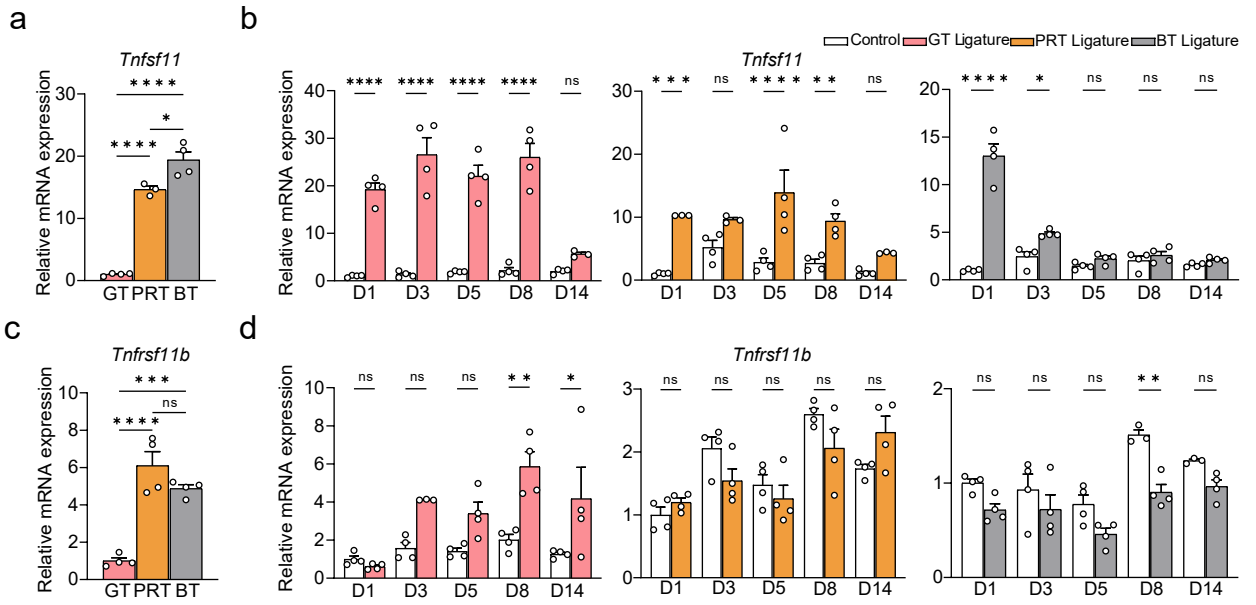

Supplementary Fig. 3 Tnfsf11 and Tnfrsf11b expression in the three tissues. | **a, c** mRNA expression of *Tnfsf11* (**a**) and *Tnfrsf11b* (**c**) on the control side of the three tissues (on Day 1; GT = 1; *n* = 3 or 4). **b, d** Temporal changes in mRNA expression of Tnfsf11 (**b**) and Tnfrsf11b (**d**) in the three tissues (Control Day 1 of each tissue = 1; *n* = 3 or 4). D1: Day 1; D3: Day 3; D5: Day 5; D8: Day 8; D14: Day 14. Data are presented as the mean ± SEM. *P < 0.05; **P < 0.01; ***P < 0.001; ****P < 0.0001; ns, P > 0.05; by one-way ANOVA with multiple comparisons via Tukey's test (**a, c**); and two-way ANOVA with multiple comparisons via Šídák's method (**b, d**). The obvious outliers were evaluated and excluded by Grubb's test (α = 0.05). The exact P values are shown in Supplementary Table 3.

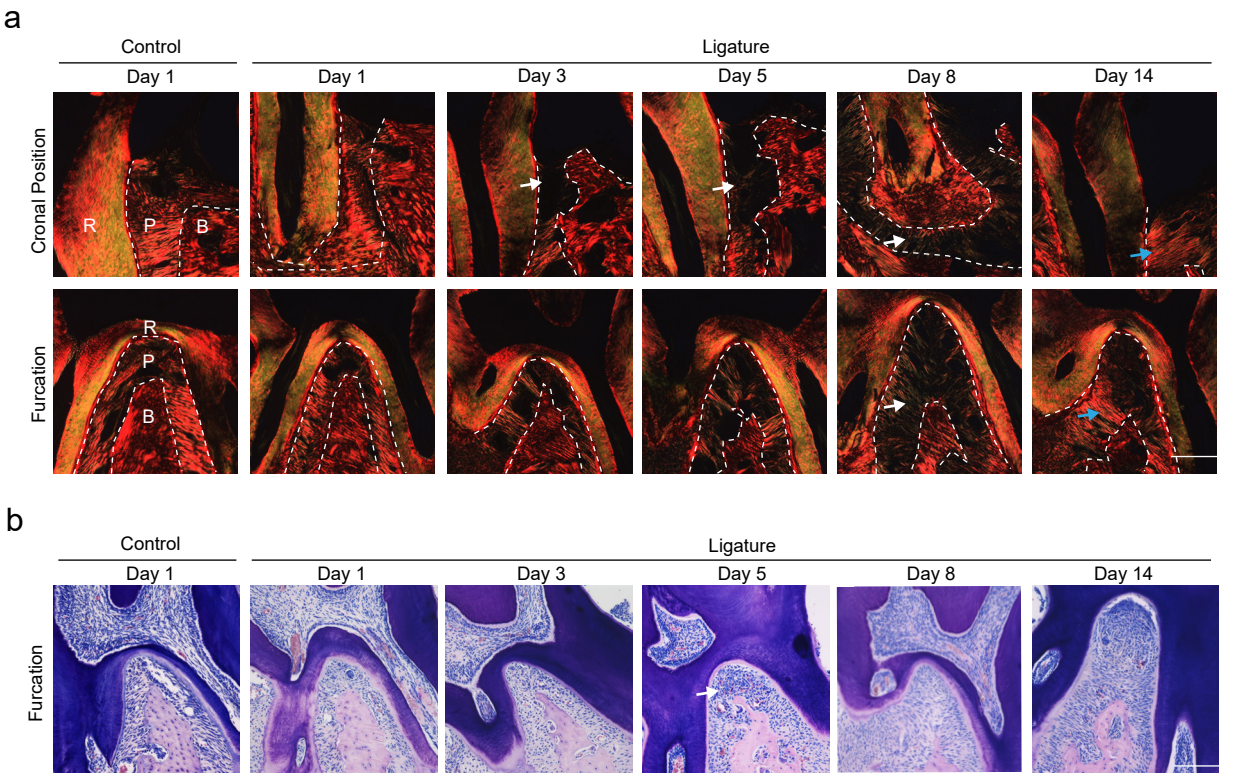

Supplementary Fig. 4 Temporal histological analysis of the pathogenesis. | **a** Representative Picro-Sirius red staining images in the second molar's coronal and furcation region. The tissues are divided by white dotted lines into R, P, and B. The white arrows indicate the destruction of type I collagen fibers. The blue arrows indicate the regeneration of type I collagen fibers. R: root; P: periodontal ligament and connective tissue; B: alveolar bone. Scale bar, 60 μm. **b** Representative Giemsa staining images in the second molar's furcation region. The white arrow indicates the apparent angiogenesis in the periodontal ligament area on Day 5. Scale bar, 60 μm.

Supplementary Fig. 5

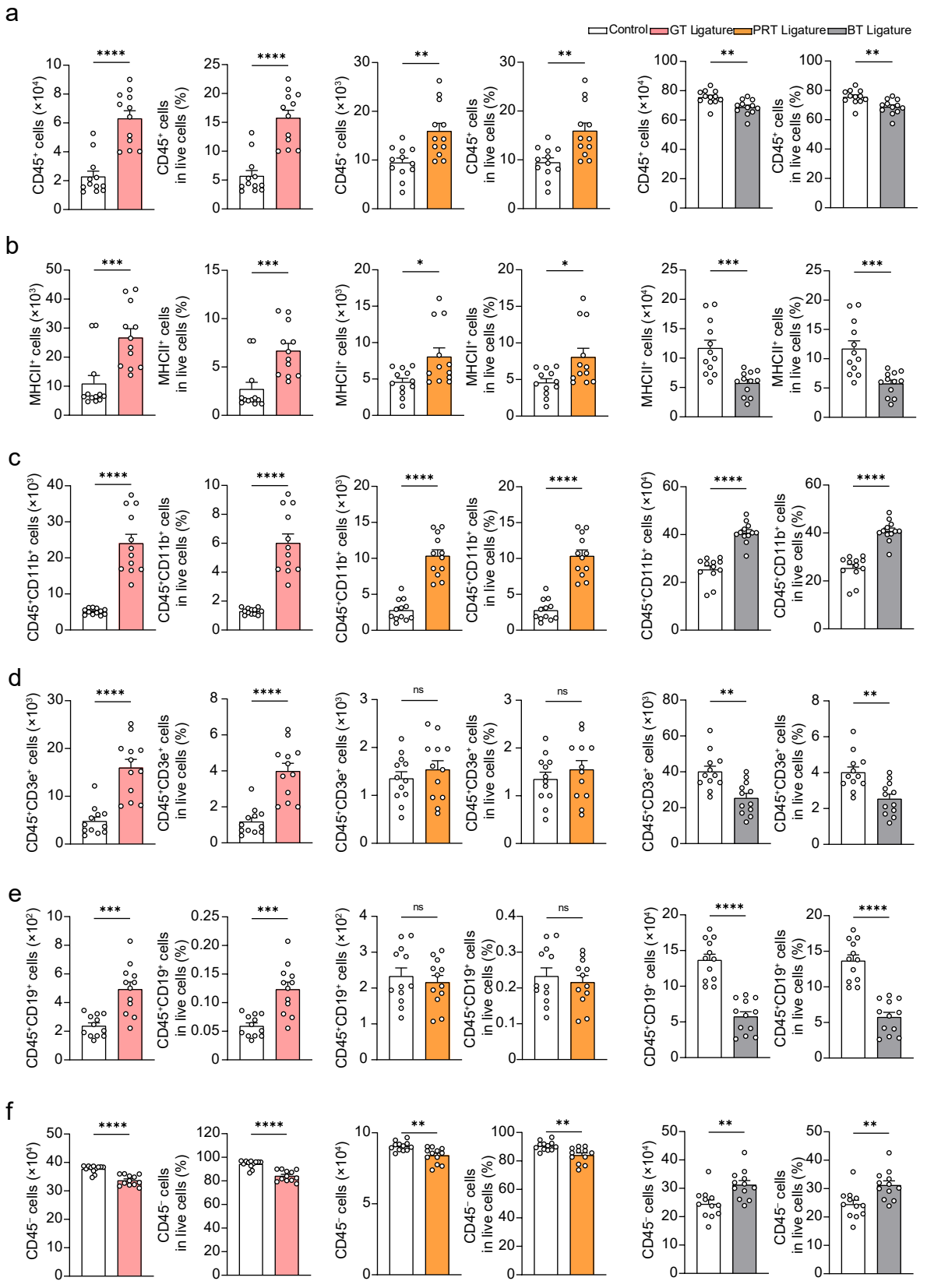

Supplementary Fig. 5 Cell component alteration in three tissues. | The number and percentages of $CD45^+$ (**a**), $MHCII^+$ (**b**), $CD45^+CD3\varepsilon^+$ (**c**), $CD45^+CD19^+$ (**d**), $CD45^+CD11b^+$ (**e**), and $CD45^-$ (**f**) cells are shown horizontally by the tissue type (*n* = 12). Data are presented as the mean ± SEM. *P < 0.05; **P < 0.01; ***P < 0.001; ****P < 0.0001; ns, P > 0.05; by Welch's t-test. The exact P values are shown in Supplementary table 3.

Supplementary Fig. 6

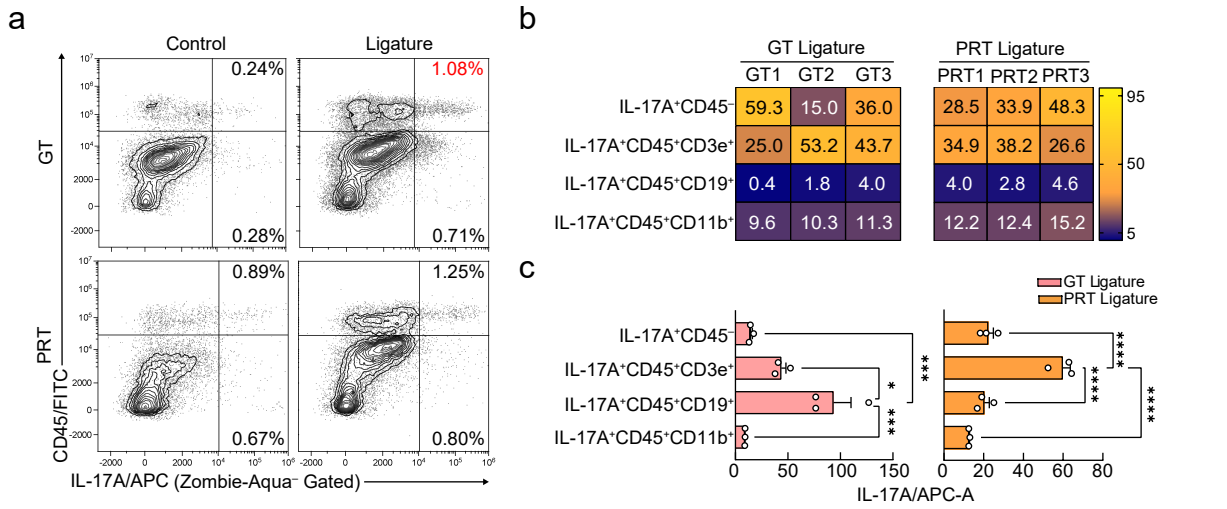

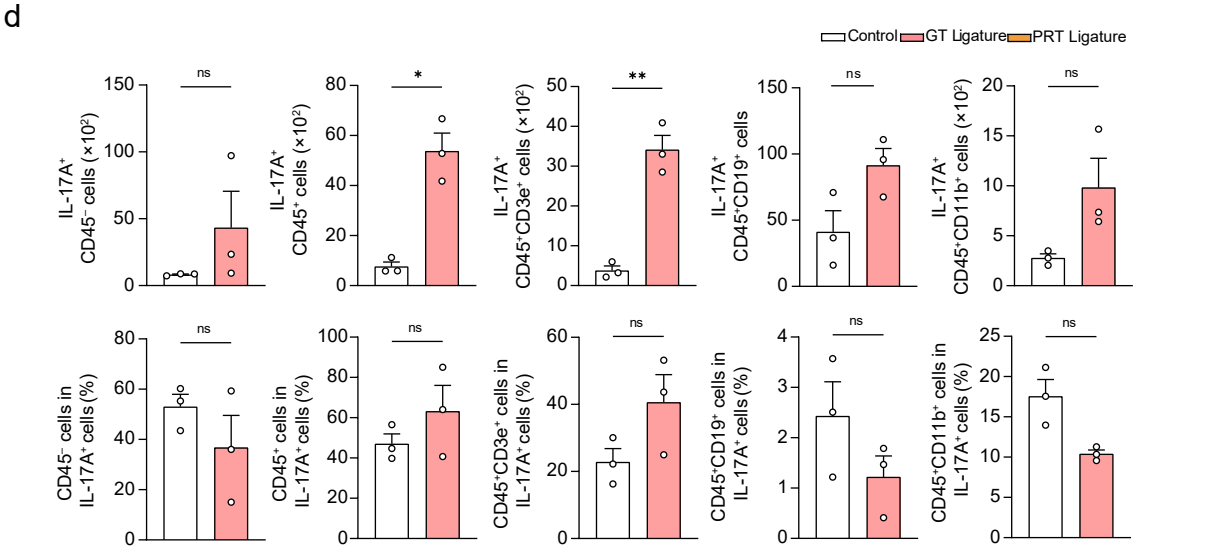

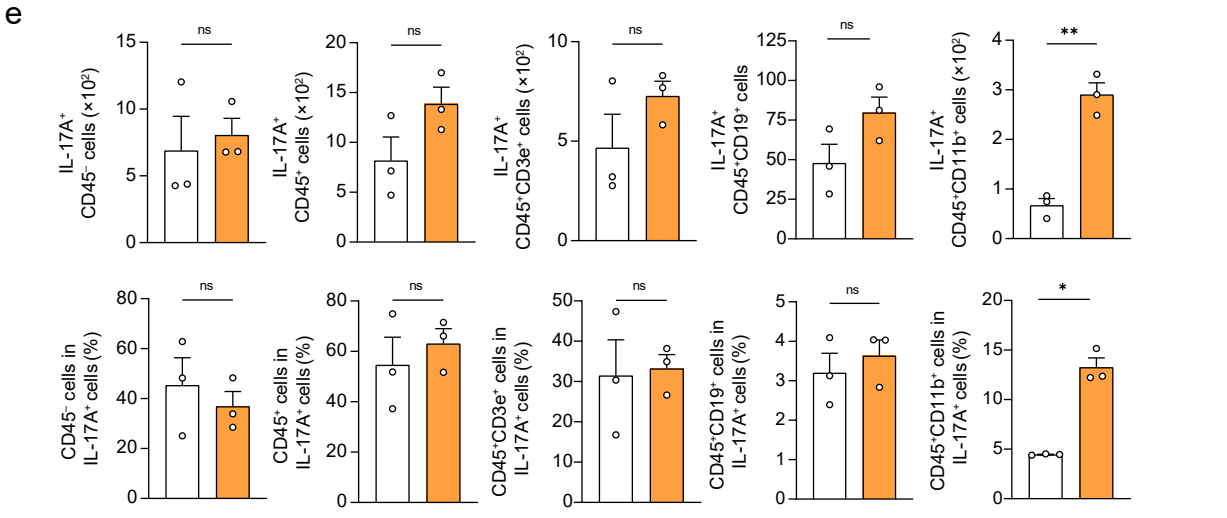

Supplementary Fig. 6 Source of IL-17A in GT and PRT in IP. | **a** Changes in IL-17A$^+$ cells in GT and PRT with or without ligature placement. A representative contour plot is shown, and the percentages shown in the gates are the mean of three individual experiments. **b** Heat map of the positive percentage of different IL-17A$^+$ lineage in ligatured GT and PRT. Data from three independent experiments are shown (*n* = 3, GT/PRT 1, 2, 3). **c** MFI (median fluorescence intensity) of the different IL-17A$^+$ lineages in ligatured GT and PRT (*n* = 3). **d, e** Changes in the cell number and percentages (in IL-17A$^+$ or IL-17A$^+$CD45$^+$ cells) of different IL-17A$^+$ lineages in GT (**d**) and PRT (**e**) are shown perpendicularly (*n* = 3). Data are presented as the mean ± SEM except for **a**. *P < 0.05; **P < 0.01; ***P < 0.001; ****P < 0.0001; ns, P > 0.05; by one-way ANOVA with multiple comparisons via Tukey's test (**c**); and Welch's t-test (**d, e**). The exact P values are shown in Supplementary Table 3.

Supplementary Fig.7

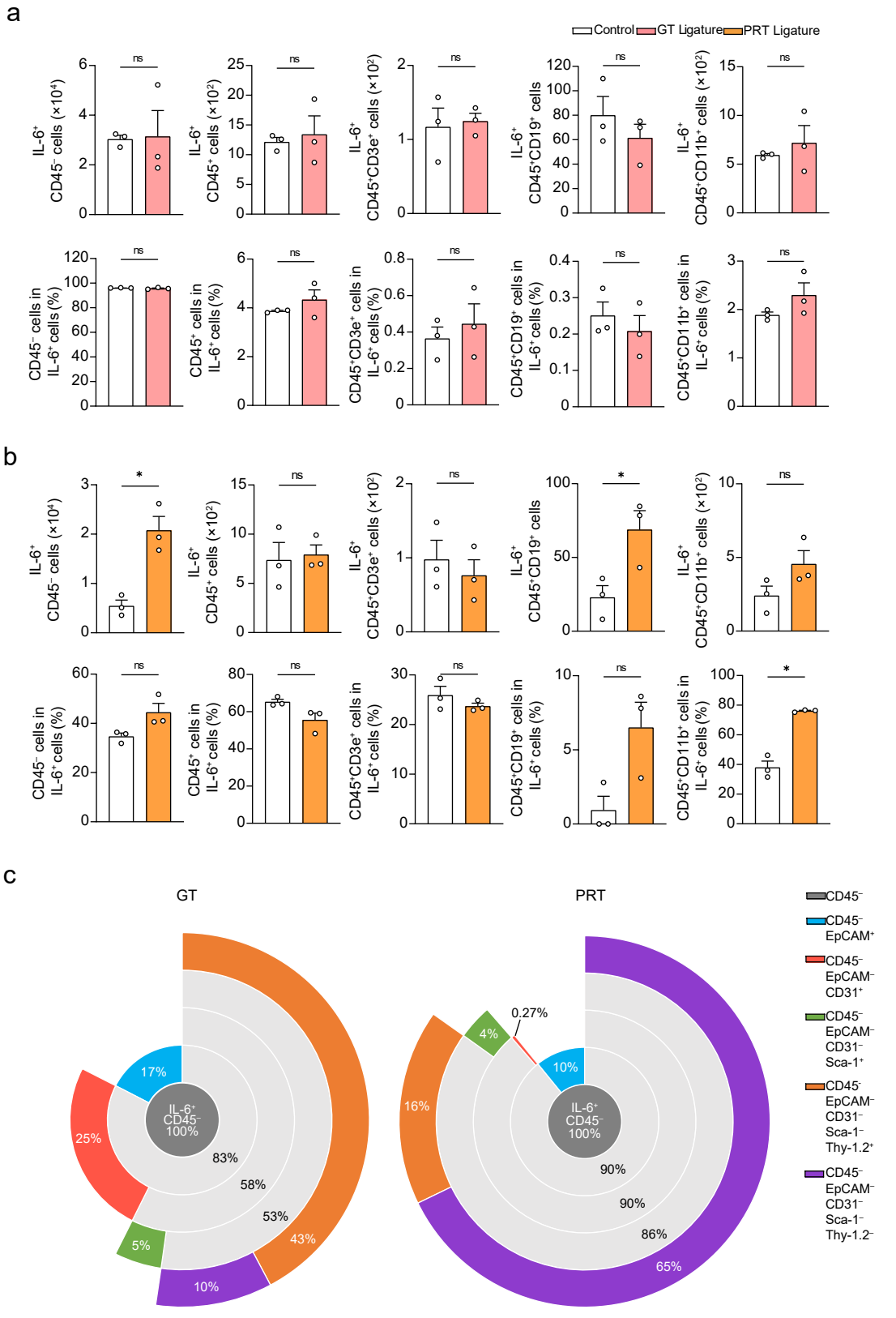

Supplementary Fig. 7 Source of IL-6 in GT and PRT in IP. | **a, b** Changes in the cell number and percentages (in IL-6$^+$ or IL-6$^+$CD45$^+$ cells) of different IL-6$^+$ lineages in GT (**a**) and PRT (**b**) are shown perpendicularly (*n* = 3). **c** Sunburst showing the composition of IL-6$^+$CD45$^-$ cells in GT and PRT. The percentages shown in the populations are the mean of three individual experiments. Data are presented as the mean ± SEM except for **c**. *P < 0.05; **P < 0.01; ***P < 0.001; ****P < 0.0001; ns, P > 0.05; by Welch's t-test. The exact P values are shown in Supplementary Table 3.

Supplementary Fig. 8

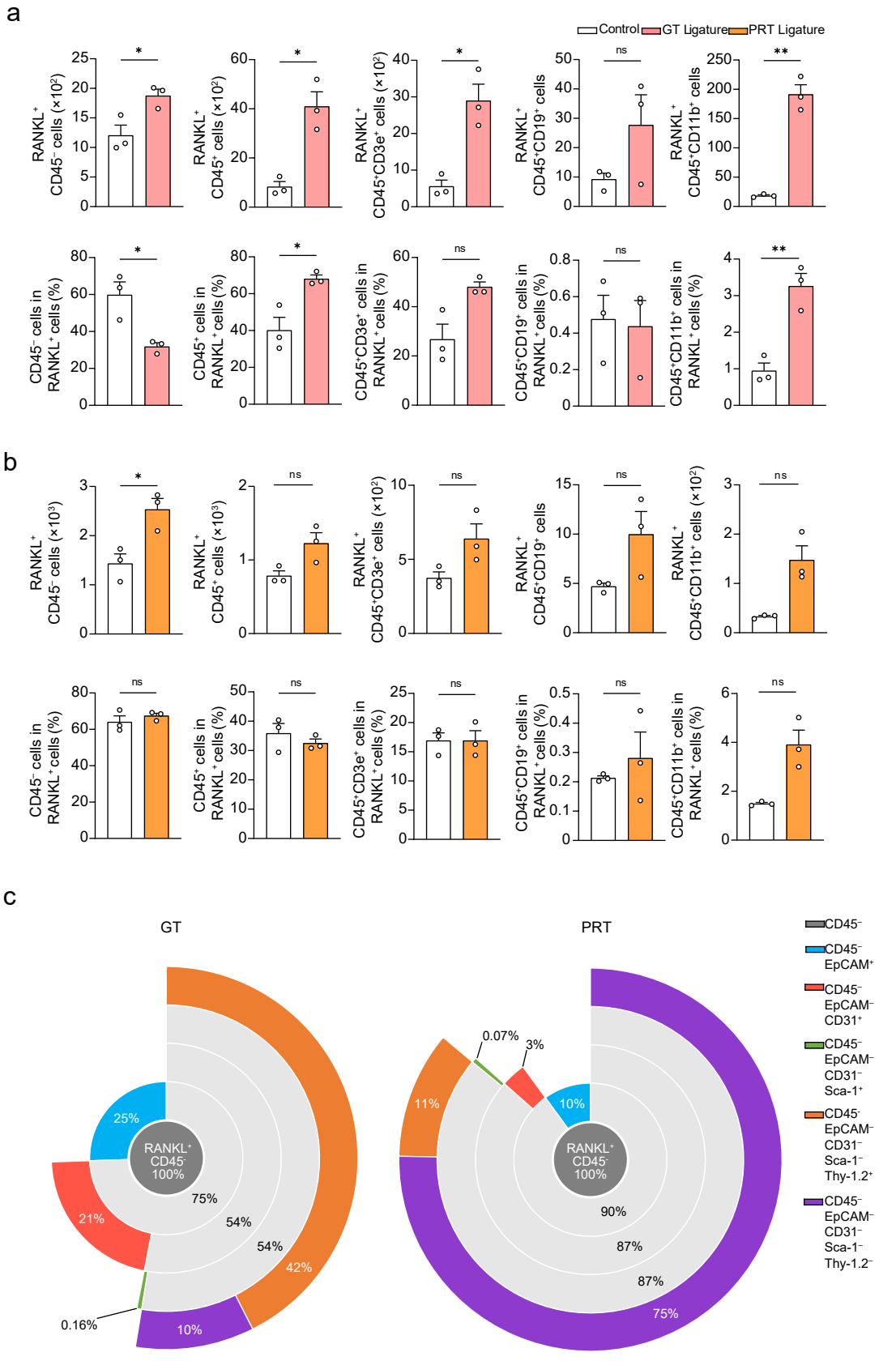

Supplementary Fig. 8 Source of RANKL in GT and PRT in IP. | **a, b** Changes in the cell number and percentages (in $RANKL^+$ or $RANKL^+CD45^+$ cells) of different $RANKL^+$ lineages in GT (**a**) and PRT (**b**) are shown perpendicularly (n = 3). c Sunburst showing the composition of $RANKL^+CD45^-$ cells in GT and PRT. The percentages shown in the populations are the mean of three individual experiments. Data are presented as the mean ± SEM except for c. *P < 0.05; **P < 0.01; ***P < 0.001; ****P < 0.0001; ns, P > 0.05; by Welch's t-test. The exact P values are shown in Supplementary Table 3.

Supplementary Fig. 9

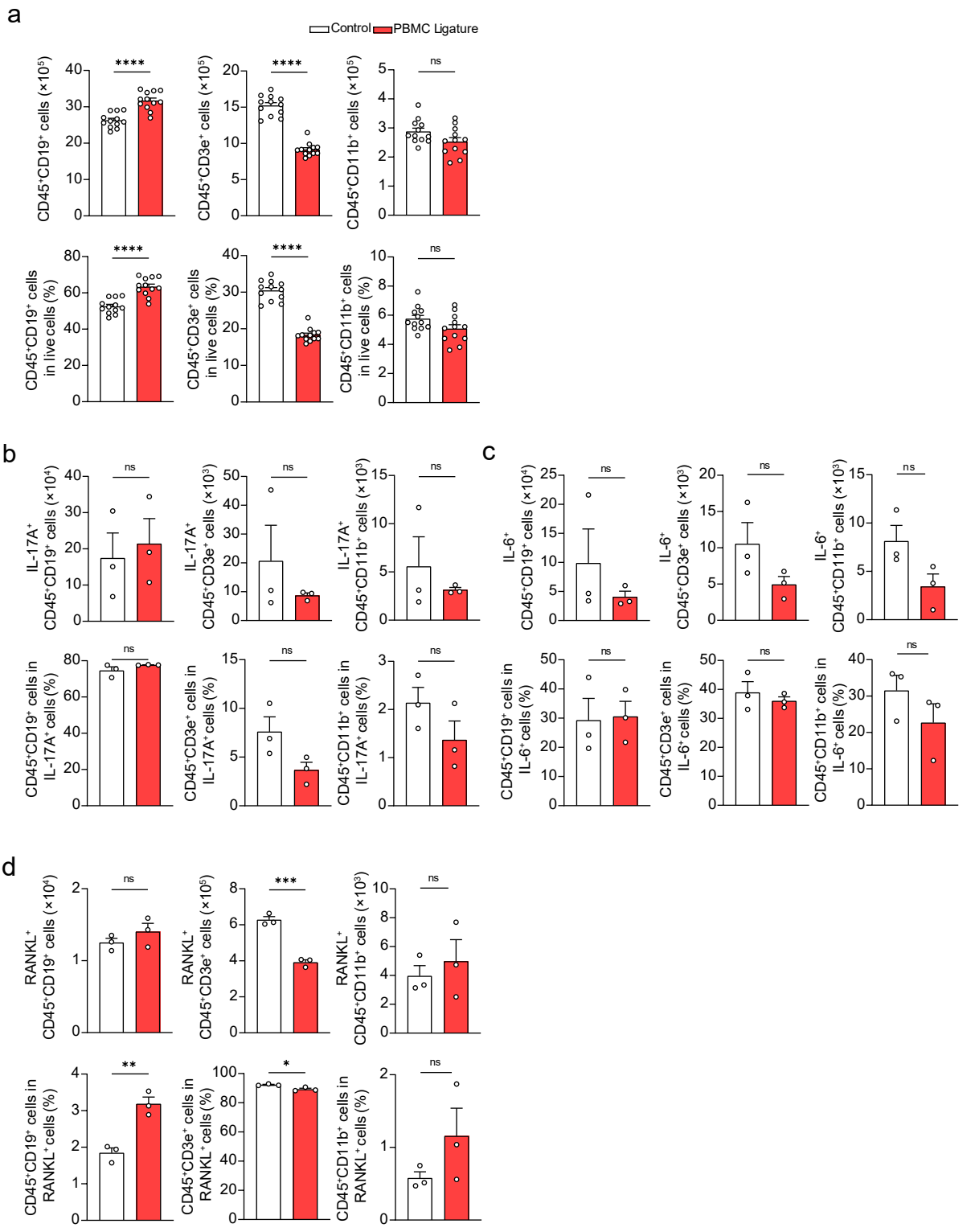

Supplementary Fig. 9 Changes in the composition of PBMC and its possible source in inflammation-related cytokines in IP. | **a** Changes in the number and percentages (in live cells) of $CD45^+CD3\varepsilon^+$, $CD45^+CD19^+$, and $CD45^+CD11b^+$ cells are shown perpendicularly. **b–d** Changes in the cell number and percentages (in $CD45^+$ cells) of different $IL\text{-}17A^+$ (**b**), $IL\text{-}6^+$ (**c**), and $RANKL^+$ (**d**) lineages in PBMC are shown perpendicularly (*n* = 3). PBMC: peripheral blood mononuclear cell. Data are presented as the mean ± SEM. *P < 0.05; **P < 0.01; ***P < 0.001; ****P < 0.0001; ns, P > 0.05; by Welch's t-test. The exact P values are shown in Supplementary Table 3.

Supplementary Fig. 10

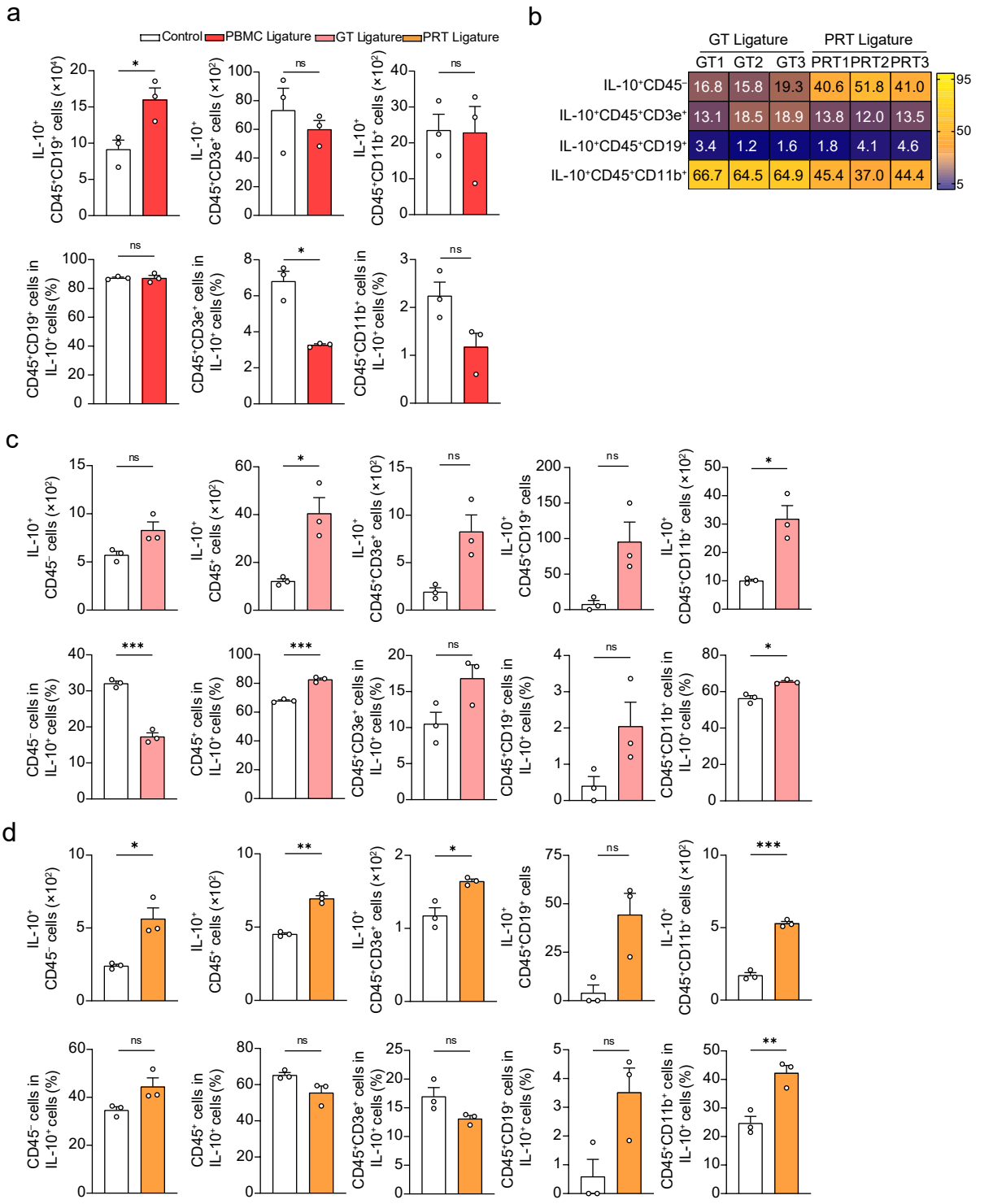

Supplementary Fig. 10 Source of IL-10 in IP. | **a** Changes in the cell number and percentages (in IL-10$^+$CD45$^+$ cells) of the different IL-10$^+$ lineages in PBMC are shown perpendicularly (*n* = 3). **b** Heat map of the positive percentage of different IL-10$^+$ lineages in the ligatured GT and PRT. The data from three independent experiments are shown (*n* = 3, GT/PRT 1, 2, 3). **c, d** Changes in the cell number and percentages (in IL-10$^+$ or IL-10$^+$CD45$^+$ cells) of different IL-10$^+$ lineages in GT (**c**) and PRT (**d**) are shown perpendicularly (*n* = 3). Data are presented as the mean ± SEM. *P < 0.05; **P < 0.01; ***P < 0.001; ****P < 0.0001; ns, P > 0.05; by Welch's t-test. The exact P values are shown in Supplementary Table 3.

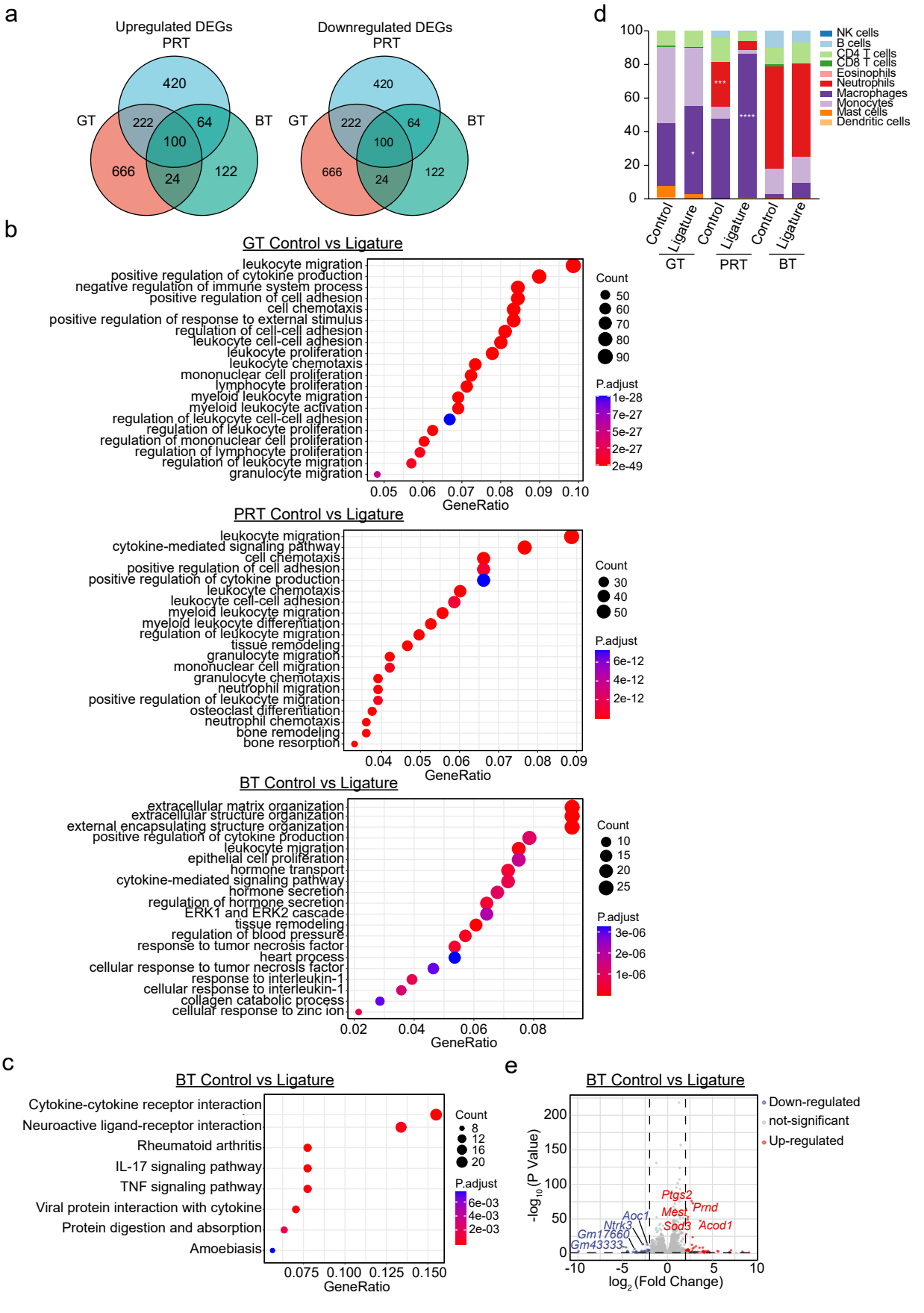
a
Upregulated DEGs
PRT
420
GT
222
64
BT
100
666
24
122
Downregulated DEGs
PRT
420
GT
222
64
BT
100
666
24
122
d
100
80
60
40
20
0
NK cells
B cells
CD4 T cells
CD8 T cells
Eosinophils
Neutrophils
Macrophages
Monocytes
Mast cells
Dendritic cells
Control
Ligature
Control
Ligature
Control
Ligature
GT
PRT
BT
b
GT Control vs Ligature
leukocyte migration
positive regulation of cytokine production
negative regulation of immune system process
positive regulation of cell adhesion
cell chemotaxis
positive regulation of response to external stimulus
regulation of cell-cell adhesion
leukocyte cell-cell adhesion
leukocyte proliferation
leukocyte chemotaxis
mononuclear cell proliferation
lymphocyte proliferation
myeloid leukocyte migration
myeloid leukocyte activation
regulation of leukocyte cell-cell adhesion
regulation of leukocyte proliferation
regulation of mononuclear cell proliferation
regulation of lymphocyte proliferation
regulation of leukocyte migration
granulocyte migration
0.05 0.06 0.07 0.08 0.09 0.10
GeneRatio
Count
50
60
70
80
90
P.adjust
1e-28
7e-27
5e-27
2e-27
2e-49
PRT Control vs Ligature
leukocyte migration
cytokine-mediated signaling pathway
cell chemotaxis
positive regulation of cell adhesion
positive regulation of cytokine production
leukocyte chemotaxis
leukocyte cell-cell adhesion
myeloid leukocyte migration
myeloid leukocyte differentiation
regulation of leukocyte migration
tissue remodeling
granulocyte migration
mononuclear cell migration
granulocyte chemotaxis
neutrophil migration
positive regulation of leukocyte migration
osteoclast differentiation
neutrophil chemotaxis
bone remodeling
bone resorption
0.04 0.05 0.06 0.07 0.08 0.09
GeneRatio
Count
30
40
50
P.adjust
6e-12
4e-12
2e-12
BT Control vs Ligature
extracellular matrix organization
extracellular structure organization
external encapsulating structure organization
positive regulation of cytokine production
leukocyte migration
epithelial cell proliferation
hormone transport
cytokine-mediated signaling pathway
hormone secretion
regulation of hormone secretion
ERK1 and ERK2 cascade
tissue remodeling
regulation of blood pressure
response to tumor necrosis factor
heart process
cellular response to tumor necrosis factor
response to interleukin-1
cellular response to interleukin-1
collagen catabolic process
cellular response to zinc ion
0.02 0.04 0.06 0.08
GeneRatio
Count
10
15
20
25
P.adjust
3e-06
2e-06
1e-06
c
BT Control vs Ligature
Cytokine-cytokine receptor interaction
Neuroactive ligand-receptor interaction
Rheumatoid arthritis
IL-17 signaling pathway
TNF signaling pathway
Viral protein interaction with cytokine
Protein digestion and absorption
Amoebiasis
0.075 0.100 0.125 0.150
GeneRatio
Count
8
12
16
20
P.adjust
6e-03
4e-03
2e-03
e
BT Control vs Ligature
Down-regulated
not-significant
Up-regulated
200
150
100
50
0
-log10 (P Value)
Ptgs2
Prnd
Mest
Sod3
Acod1
Aoc1
Ntrk3
Gm17660
Gm43333
-10 -5 0 5 10
log2 (Fold Change)

Supplementary Fig. 11 Comprehensive analysis of the three tissues in IP. | **a** Venn diagrams of DEGs in three tissues. **b** GO term (BP) enrichment analysis by the upregulated DEGs in the three tissues. The top 20 terms are presented with their expression counts and adjusted P value. **c** KEGG pathway enrichment analysis by the upregulated DEGs in BT. The top 20 terms are presented with their expression counts and adjusted P value. **d** Immune cell component analysis by ImmuCC. The population percentage was compared between the control and ligature samples within each tissue. **e** Volcano plots of the DEGs in BT. The top 5 genes with the highest adjusted P value are annotated. *P < 0.05; **P < 0.01; ***P < 0.001; ****P < 0.0001; ns, P > 0.05; by two-way ANOVA with multiple comparisons via Tukey's test (**b**). The exact P values are shown in Supplementary Table 3.

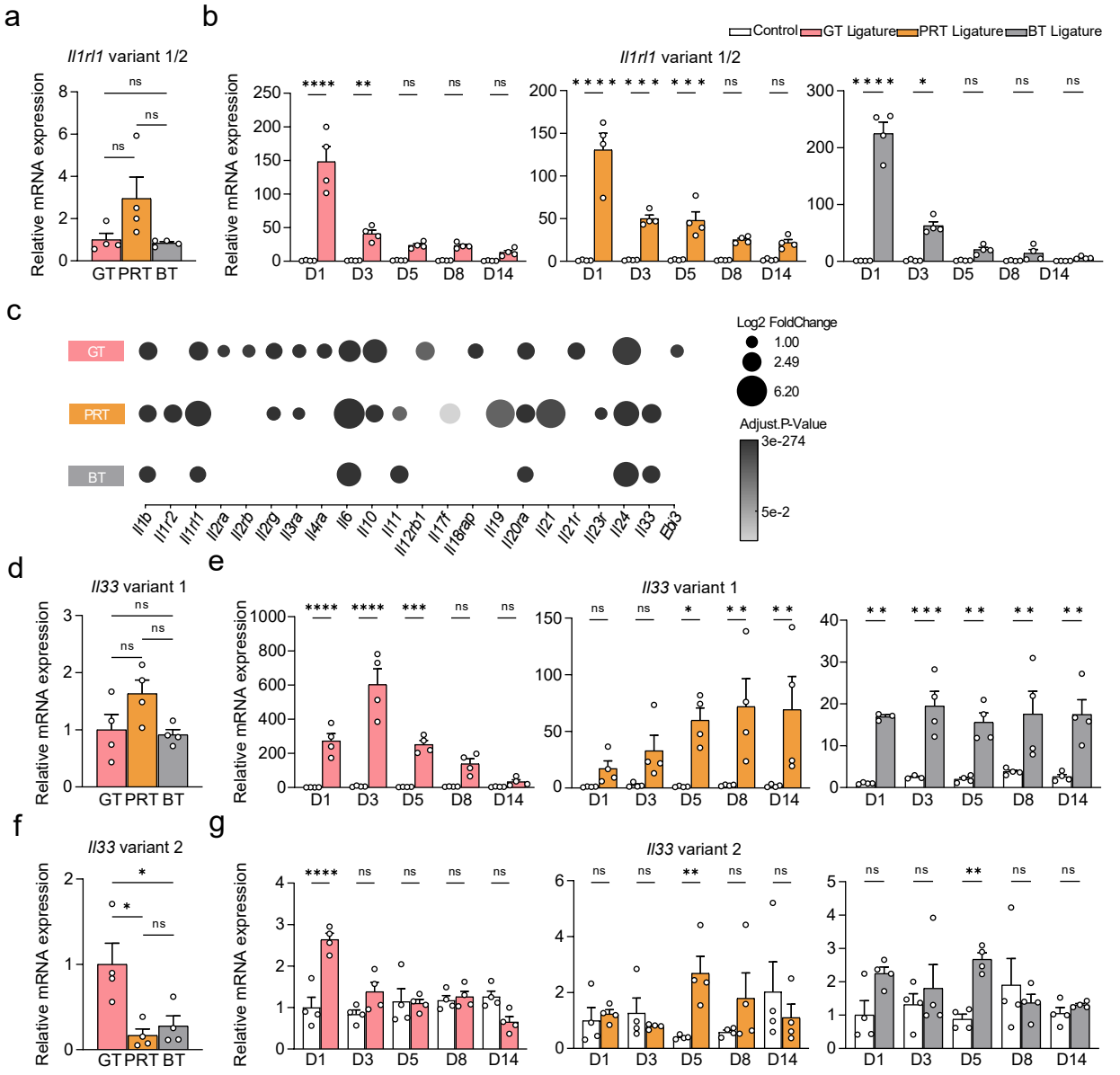

Supplementary Fig. 12 Involvement of different transcriptional variants of the IL-33/ST2 axis. | a, d, f mRNA transcriptional variant expression of *Il1rl1* variant 1/2 (**a**), *Il33* variant 1 (**d**), and *Il33* variant 2 (**f**) on the control side of the three tissues (Control Day 1 of each tissue = 1; *n* = 3 or 4). **b, e, g** Temporal change in mRNA transcriptional variant expression of *Il1rl1* variant 1/2 (**b**), *Il33* variant 1 (**e**), and *Il33* variant 2 (**g**) in the three tissues (Control Day 1 of each tissue = 1; *n* = 3 or 4). **c** Log2 fold change of interleukin-related mRNA in the RNA-seq data of the three tissues. The fold changes calculated from the raw expression counts via DEseq2 are presented with their adjusted P value. The data for fold changes fewer than 1 or adjusted P value over 0.1 are not shown. Data are presented as the mean ± SEM. *P < 0.05; **P < 0.01; ***P < 0.001; ****P < 0.0001; ns, P > 0.05; by one-way ANOVA with multiple comparisons via Tukey's test (**a, d, f**); and two-way ANOVA with multiple comparisons via Šídák's method (**b, e, g**). The obvious outliers were evaluated and excluded by Grubb's test (α = 0.05). The exact P values are shown in Supplementary Table 3.

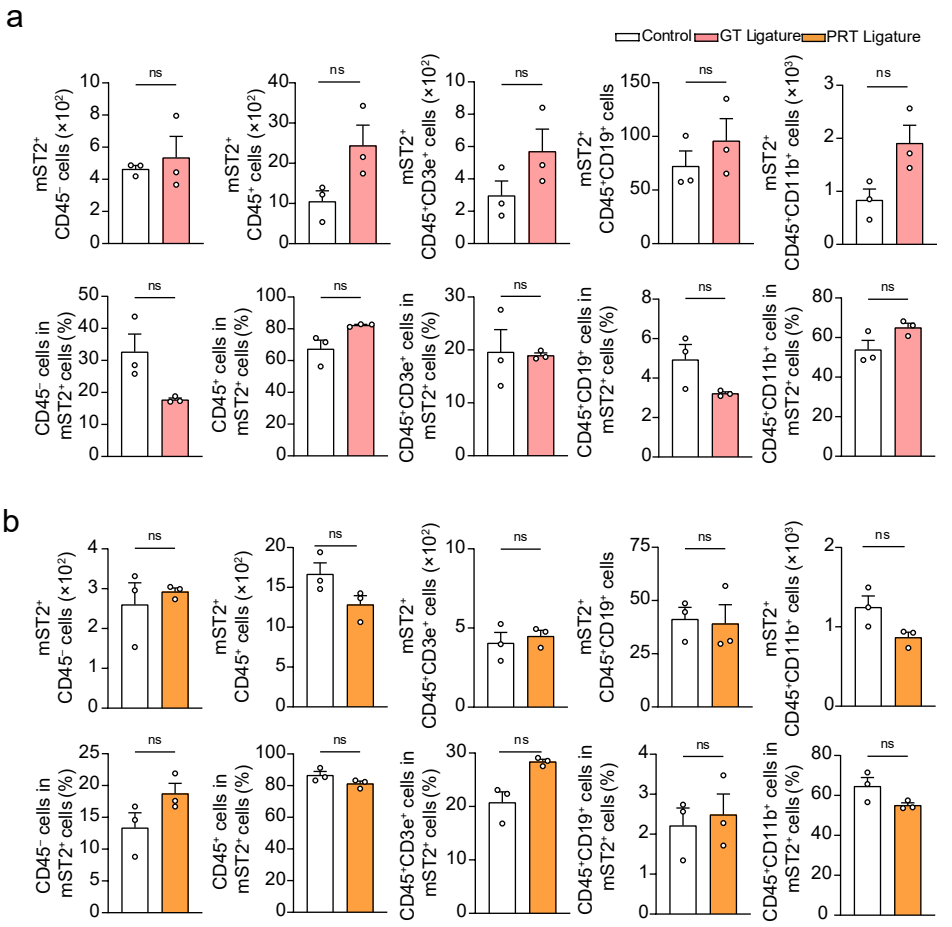

Supplementary Fig. 13 mST2⁺ cells in GT and PRT in IP. | Changes in the cell number and percentages (in mST2⁺ or mST2⁺CD45⁺ cells) of the different mST2⁺ lineages in GT (**a**) and PRT (**b**) are shown perpendicularly (*n* = 3). Data are presented as the mean ± SEM. *P < 0.05; **P < 0.01; ***P < 0.001; ****P < 0.0001; ns, P > 0.05; by Welch's t-test. The exact P values are shown in Supplementary Table 3.

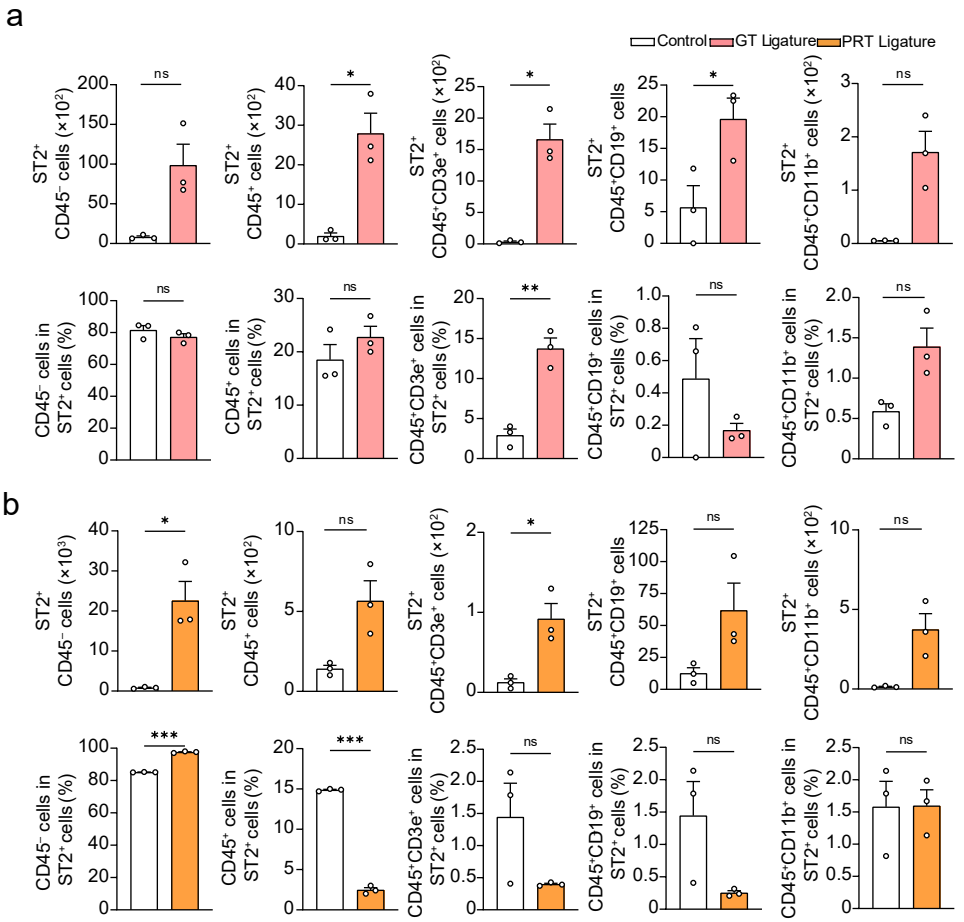

Supplementary Fig. 14 ST2⁺ cells in GT and PRT in IP. | Changes in the cell number and percentages (in ST2⁺ or ST2⁺CD45⁺ cells) of the different ST2⁺ lineages in GT (**a**) and PRT (**b**) are shown perpendicularly (*n* = 3). Data are presented as the mean ± SEM. *P < 0.05; **P < 0.01; ***P < 0.001; ****P < 0.0001; ns, P > 0.05; by Welch's t-test. The exact P values are shown in Supplementary Table 3.

Supplementary Fig. 15

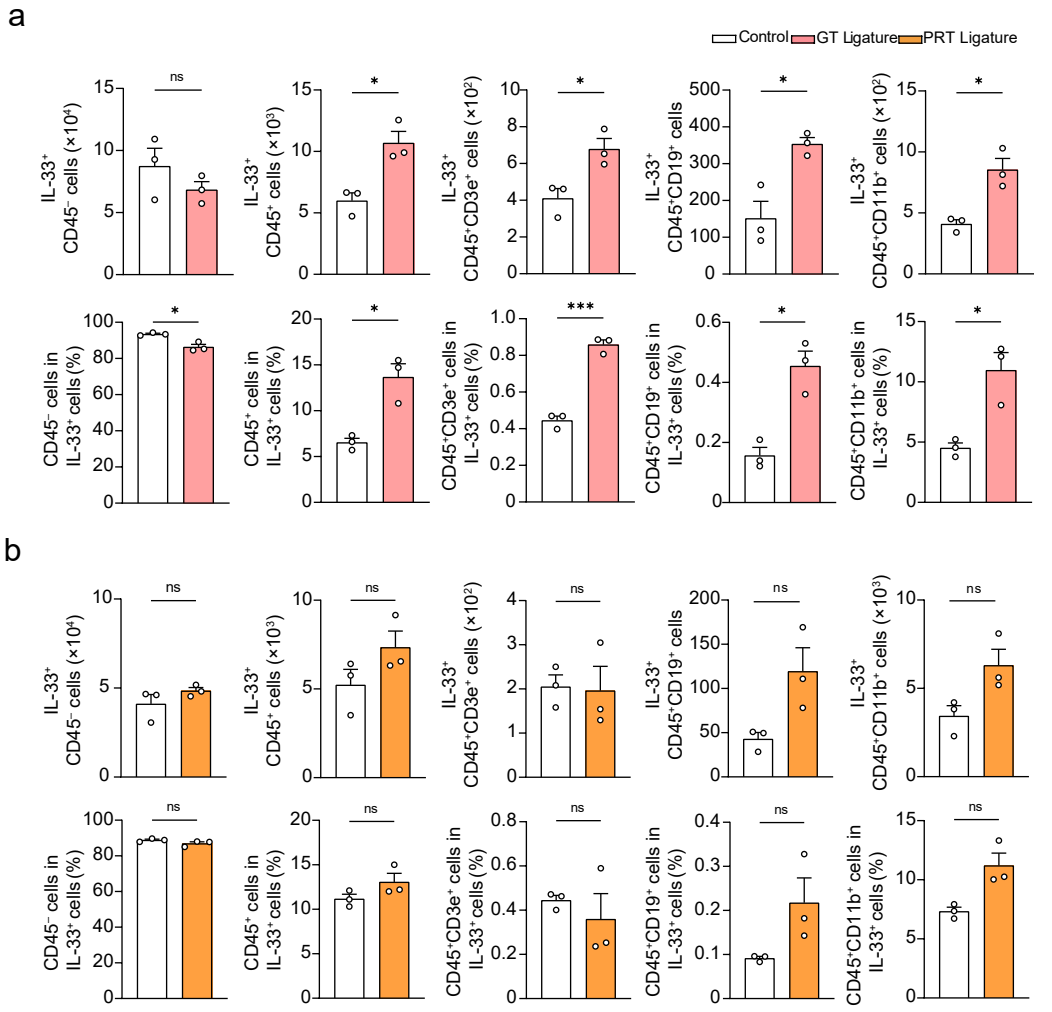

Supplementary Fig. 15 Source of IL-33 in GT and PRT in IP. | Changes in the cell number and percentages (in IL-33$^+$ or IL-33$^+$CD45$^+$ cells) of the different IL-33$^+$ lineages in GT (**a**) and PRT (**b**) are shown perpendicularly (n = 3). Data are presented as the mean ± SEM. *P < 0.05; **P < 0.01; ***P < 0.001; ****P < 0.0001; ns, P > 0.05; by Welch's t-test. The exact P values are shown in Supplementary Table 3.

Supplementary Fig. 16

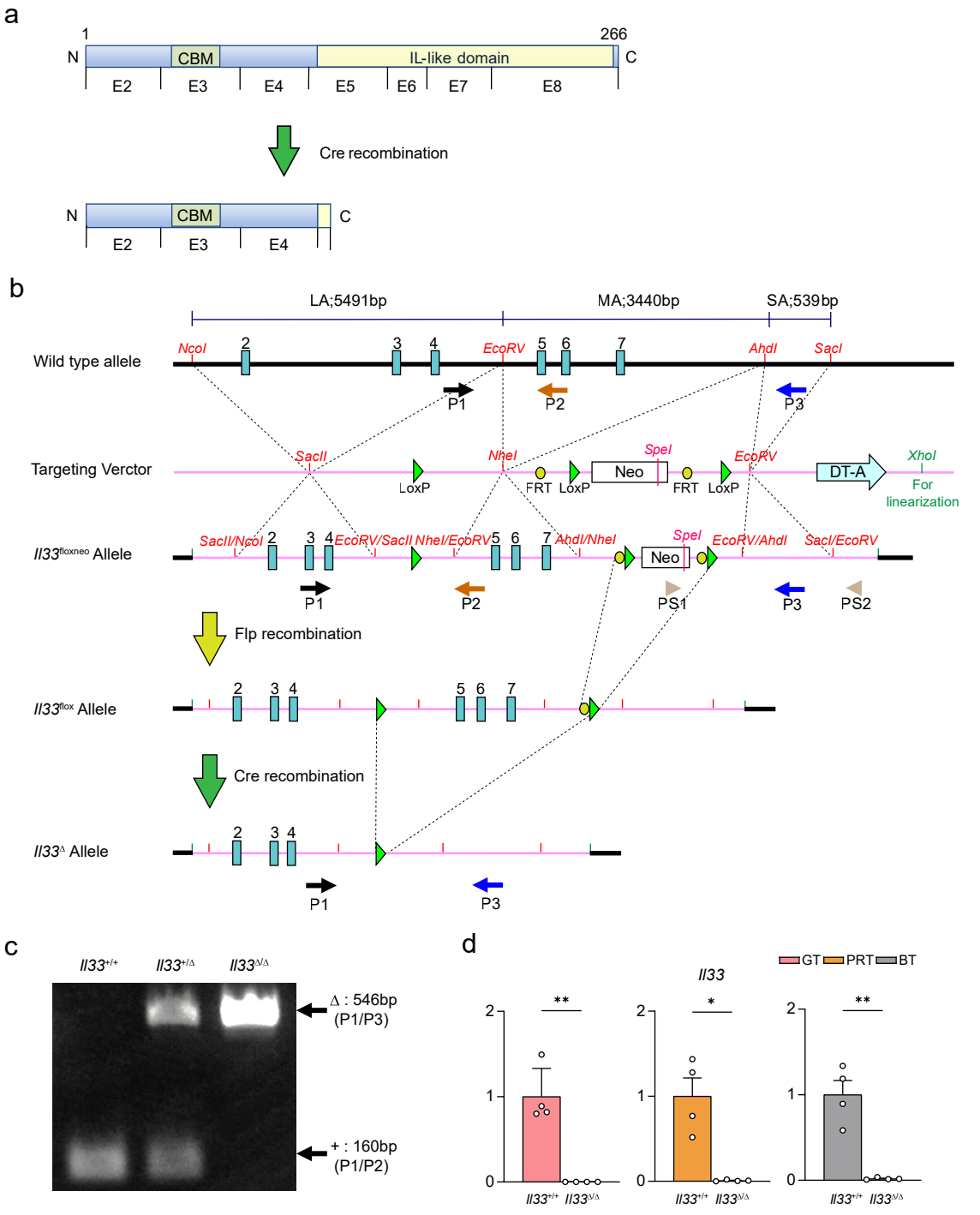

Supplementary Fig. 16 Conditional gene-targeting of *Il33*. | **a** Representation of the functional extracellular IL-like domain of IL-33 binding to its receptor. Cre-mediated excision of exons 5 to 7 of the *Il33* gene led to a loss of the IL-like domain of IL-33. CBM: chromatin binding motif. E: exon. **b** Targeting strategy to generate *Il33* conditional mutant mice. The genomic structure of the wild-type *Il33* gene, the targeting vector and the targeted alleles are indicated. Exons 5 to 7 are flanked by *loxP* sequences; the *Neo* cassette is flanked by *frt* sequences. The modified *Il33* locus after homologous recombination ($Il33^{floxNeo}$ allele), the *Il33* gene after excision of the *Neo* cassette following expression of Flp recombinase ($Il33^{flox}$ allele), and the deleted *Il33* gene after Cre-mediated excision of the exons ($Il33^{\Delta}$ allele) are shown. The arrows below the diagram of the wild-type allele indicate the positions of the primers (P1, P2 and P3) used for PCR genotyping. **c** Genotyping PCR of tail genomic DNA using the primer pairs shown in Supplementary Text 1. **d** mRNA expression of *Il33* on the control side of the different periodontal tissues between the WT and $Il33^{\Delta/\Delta}$ strains (on Day 5; each periodontal tissue of WT strain = 1; n = 4). Repeated data are presented as the mean ± SEM. *P < 0.05; **P < 0.01; ***P < 0.001; ****P <

Supplementary Fig. 17

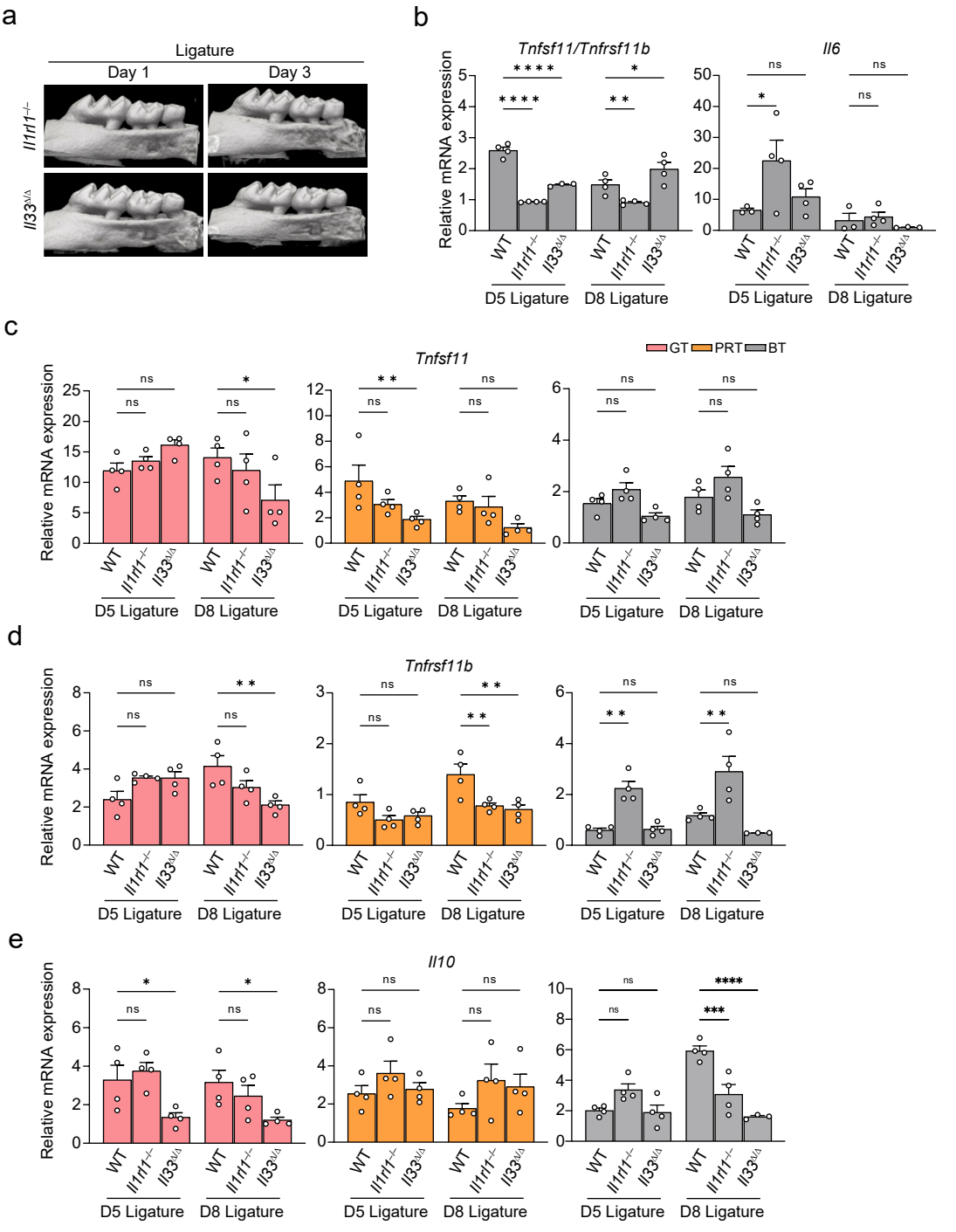

Supplementary Fig. 17 Additional information for analyzing the mechanism of the protective role of the IL-33/ST2 axis. | **a** Representative maxillary μCT images of KO mice on the ligature sides on Day 1 and Day 3 (*n* = 4). Scale bar, 1 mm. b Temporal changes in the *Tnfsf11/Tnfrsf11b* mRNA ratio and mRNA expression of *Il6* in BT among the mouse strains (control Day 1 of each tissue = 1; *n* = 3 or 4). **c–e** Temporal changes in *Tnfsf11* (**c**), *Tnfrsf11b* (**d**), and *Il10* (**e**) in the three tissues among the mouse strains (control Day 5 of each tissue in each strain = 1; *n* = 3 or 4). Data are presented as the mean ± SEM. *P < 0.05; **P < 0.01; ***P < 0.001; ****P < 0.0001; ns, P > 0.05; by two-way ANOVA with multiple comparisons via Dunnett's test. The obvious outliers were evaluated and excluded by Grubb's test (α = 0.05). The exact P values are shown in Supplementary Table 3.

Generation of mice carrying the *Il33* conditional allele.

All fragments for the construction of the *Il33* targeting vector were derived from a BAC clone (RP23-381K18: BACPAC Resource Center) by restriction digestion and subcloned into a pBluescript II vector. The homology arms were cloned into a targeting vector backbone containing PGK-*neo* and DTA-positive and -negative selection cassettes (pLFNeo-DTA vector) (Supplementary Fig. 17b). The long arm was excised as a *NcoI/EcoRV* fragment (5.5 kb) from the pBluescript II vector including all of the homology arms of *Il33*, and cloned into the *SacII* sites of a pLFNeo-DTA vector upstream of the *neo* selection cassette, which was flanked by *frt* sites. For construction of the middle arm, a fragment encompassing exon 5 to 7 of *Il33* was excised as the *EcoRV/AhdI* fragment (3.4 kb), and cloned into the *NheI* site of the pLFNeo-DTA vector just upstream of the *neo* selection cassette so as to flank exon 5 to 7 with *loxP* sites. The short arm was excised as the *AhdI/SacI* fragment (0.5 kb), then cloned into the *EcoRV* sites of the pLFNeo-DTA vector upstream of the DTA cassette to give rise to the final targeting vector for the $Il33^{floxNeo}$ allele. The targeting vector was linearized with *XhoI* and electroporated into A9 embryonic stem (ES) cells. A9 ES cells were derived from the 129 and C57BL/6 hybrid strain (Nakashima et al. *Nat Med* 2011). After 8–9 days of G418 selection, resistant single colonies were picked and transferred onto primary embryonic fibroblast cells acting as feeder cells, and expanded to allow diagnosis of homologous recombination. Potential recombinant clones were detected by genomic PCR. The forward primer (PS1: the construct-specific primer, 5'-AGACTGCCTTGGGAAAAG-3') binds within the *neo* selection cassette region, the reverse primer (PS2: the locus-specific primer, 5'-CCCTGCCAATGAATACTG-3') binds to a unique region outside the short arm of the targeting vector and within the endogenous locus. The *loxP* site between the long and middle arms was confirmed using the primer pairs (P1 and P2: described below). Approximately 2–3 out of 100 ES cell clones were identified as correctly targeted by genomic PCR. Targeted ES cells were injected into C57BL/6J blastocysts to achieve initial germ-line transmission. Chimeric male mice were crossed with C57BL/6J females to establish a line for the $Il33^{floxNeo}$ allele. Mice carrying the *frt*-flanked PGK-*neo* cassette was crossed with C57BL/6J background FLPe transgenic mice to excise the PGK-*neo* cassette and subsequently crossed to C57BL/6J mice to remove the FLPe recombinase transgene so as to generate $Il33^{flox}$ mice. In parallel, $Il33^{flox}$ mice were also crossed to C57BL/6J background *Actb-Cre* ubiquitous deleter mice to generate mice carrying a $Il33^{\Delta}$ allele (Global KO). Mice carrying the $Il33^{flox}$ or $Il33^{\Delta}$ alleles were backcrossed more than 7 generations to C57BL/6J mice. These mice were then intercrossed to generate $Il33^{flox/\Delta}$

and *Il33*$^{+/\Delta}$ mice. For mouse genotyping, genomic DNA from mouse tails was isolated by phenol/chloroform extraction and ethanol precipitation, and amplified by PCR with three primers: P1, 5'-ACATAGTTCTGCACGCTG-3'; P2, 5'-GTCCAGACCTTTTGTGGG-3'; and P3, described above. The PCR products were 160 bp (wild-type allele, primers P1/P2), 291 bp (floxed allele, primers P1/P2) and 546 bp (delta allele, primers P1/P3), showed in supplementary figure (Supplementary Fig. 16c). The *Cre* transgene was detected as a 455 bp PCR product by using the forward primer 5'-TCGCGATTATCTTCTATATCTTCAG-3' and reverse primer 5'-GCTCGACCAGTTTAGTTACCC-3'. The expression loss of normal *Il33* mRNA was further confirmed with RT-qPCR in periodontal tissues before use (Supplementary Fig. 16d).